





Orbital eccentricity in general relativity from catastrophe theory

Matteo Boschini ^{1,2,*} Nicholas Loutrel ^{1,2} Davide Gerosa ^{1,2} and Giulia Fumagalli ^{1,2}

¹*Dipartimento di Fisica “G. Occhialini”, Università degli Studi di Milano-Bicocca, Piazza della Scienza 3, 20126 Milano, Italy*

²*INFN, Sezione di Milano-Bicocca, Piazza della Scienza 3, 20126 Milano, Italy*

(Dated: November 4, 2024)

While the orbital eccentricity is a key feature of the gravitational two-body problem, providing an unambiguous definition in General Relativity poses significant challenges. Despite such foundational issue, the eccentricity of binary black holes has important implications in gravitational-wave astronomy. We present a novel approach to consistently define the orbital eccentricity in General Relativity, grounded in the mathematical field of catastrophe theory. Specifically, we identify the presence of catastrophes —i.e. breakdowns of the stationary-phase approximation— in numerical-relativity waveforms and exploit them to develop a robust and fully gauge-invariant estimator of the eccentricity. Our procedure does not require orbital fitting and naturally satisfies the Newtonian limit. We extract gauge-free eccentricity estimates from about 100 numerical-relativity simulations and find that the resulting values are systematically lower compared to those reported alongside the simulations themselves.

I. INTRODUCTION

Generic solutions to the two-body problem in Newtonian Gravity are represented by conic sections, where the orbital eccentricity e discriminates between closed and unbound orbits. Conversely, defining the eccentricity in General Relativity (GR) is a highly non-trivial problem: radiation reaction and periastron precession both lead to non-closed orbits and gauge effects are hard to eradicate [1–3].

Achieving a consistent definition of the orbital eccentricity is a pressing issue for both current and future gravitational-wave (GW) observations. For stellar-mass black-hole (BH) binaries presently targeted by LIGO/Virgo [4–7] and in the future by third-generation detectors [8, 9], the orbital eccentricity is a telltale of dynamical formation in dense environments such as clusters or disks [10, 11]. For supermassive BHs targeted by LISA [12], eccentricity is an indicator for gas accretion and recent three-body interactions [13, 14]. A BH binary detection with eccentricity that is confidently constrained away from zero is arguably one of the most long-awaited GW events, and there is already some tentative evidence in current data [15–17]. At the same time, neglecting eccentricity when present can deeply impact both the astrophysics [18] and testing-GR [19, 20] science cases of GW detectors.

Such a large scientific payoff is prompting major efforts to include eccentricity in waveform approximants — a task that remains challenging in particular when combined with spin precession [21–36]. In numerical relativity (NR), several of the public catalogs now contain simulations of eccentric binary BHs [37–42], even though with a somewhat sparse coverage of the parameter space, especially at high eccentricities. Currently, each NR effort has implemented a different definition of eccentricity. For instance, (i) the

Simulating eXtreme Spacetimes (SXS) catalog [38, 43] reports values of e which rely on a post-Newtonian (PN) fit of the orbital-frequency time derivative over the first ~ 2 orbits past junk radiation [38, 44], (ii) the Rochester Institute of Technology (RIT) group [39, 42] employs a definition $e \propto r^2 d^2 r / dt^2$ which uses the coordinate separation r and (iii) the MAYA catalog [41] defines e through the orbital frequency as $e = (\Omega - \Omega_c) / (2\Omega_c)$, where $\Omega = d\phi/dt$ with ϕ the azimuthal coordinate and Ω_c is the orbital frequency of a quasi-circular simulation [45]. All these definitions are gauge dependent due to reliance on coordinate quantities. Recent work by Shaikh *et al.* [3] (see also Ref. [40]) provides a definition that uses the (2,2)-mode waveform frequency extracted at future null infinity. While this moves the signpost toward a gauge-independent notion of the orbital eccentricity, it still requires a manual adjustment to obtain the correct Newtonian limit.

In this paper, we present a novel approach to consistently define the binary eccentricity in GR which has solid foundation in the branch of mathematics called “catastrophe theory” [46–48]. Part of the more general singularity theory, catastrophe theory deals with functions depending on both variables and parameters, characterizing how continuous and smooth variations of the latter can cause abrupt transitions of the former. These discontinuities, or “catastrophes,” are structural critical points in the function domain where the first derivative and one or more higher-order derivatives with respect to the variables vanish. Catastrophe theory has been applied to systems ranging from physics to biology [49–52]; in GW astronomy, a toy application was first presented by one of us [53]. For the dominant emission mode, our rigorous derivation reduces to the expression of Ref. [3], which is very encouraging. At the same time, with the methodology presented here, it is straightforward to extract the eccentricity from other subdominant contributions to the emitted gravitational radiation and average the result using the relative contribution to the emitted energy.

Our paper is organized as follows. In Sec. II, we derive

* m.boschini1@campus.unimib.it

the proposed definition applying the catastrophe formalism to PN analytic waveforms. In Sec. III, we present the first evidence that catastrophes are present in NR waveforms and show how these catastrophes can be exploited to obtain a solid estimator of the orbital eccentricity. We draw some concluding remarks in Sec. IV. We use geometric unit where $G = c = 1$.

II. POST-NEWTONIAN WAVEFORMS

Let us first apply our catastrophe analysis to analytic PN waveforms where the eccentricity can be confidently defined [54]. This is useful to both gain intuition and identify the correct mapping between frequency and eccentricity that can be then applied to NR.

A. Catastrophes in post-Newtonian theory

Catastrophes in the waveforms produced by eccentric binaries were first considered in Ref. [53] by decomposing

the two GW polarizations into their orbital harmonic modes and Fourier-transforming each mode individually. This is appropriate for PN waveforms but does not generalize to NR. We instead consider the complex strain and factor out the angular dependence on the inclination angle ι and the polarization angle ν using spin-weighted spherical harmonics

$$h(t) = h_+(t) - ih_\times(t) = \sum_{l=2}^{\infty} \sum_{m=-l}^l -{}_2Y_{lm}(\iota, \nu) h_{lm}(t). \quad (1)$$

We focus on three GW harmonics at the corresponding leading PN orders: $(l, m) = (2, 2)^{\text{0PN}}$, $(3, 3)^{\text{0.5PN}}$, and $(4, 4)^{\text{1PN}}$. Note that the procedure below does not depend on the sign of m . Defining $h_{lm,+} = \text{Re } h_{lm}$ and $h_{lm,\times} = \text{Im } h_{lm}$, the relevant expression for the GW polarizations are given by [55]:

$$h_{22,+}^{\text{0PN}} = -\frac{2\sqrt{\frac{\pi}{5}}M^2}{da(1-e^2)} \frac{q}{(1+q)^2} [4 \cos 2\varphi + e(5 \cos \varphi + \cos 3\varphi) + 2e^2], \quad (2)$$

$$h_{22,\times}^{\text{0PN}} = \frac{4\sqrt{\frac{\pi}{5}}M^2}{da(1-e^2)} \frac{q}{(1+q)^2} \sin \varphi [4 \cos \varphi + e(3 + \cos 2\varphi)], \quad (3)$$

$$h_{33,+}^{\text{0.5PN}} = \frac{\sqrt{\frac{\pi}{42}}M^{5/2}}{d[a(1-e^2)]^{3/2}} \frac{q(1-q)}{(1+q)^3} \sin \varphi [18 + 36 \cos 2\varphi + e(80 \cos \varphi + 20 \cos 3\varphi) + e^2(26 + 17 \cos 2\varphi + 3 \cos 4\varphi)], \quad (4)$$

$$h_{33,\times}^{\text{0.5PN}} = \frac{\sqrt{\frac{\pi}{42}}M^{5/2}}{d[a(1-e^2)]^{3/2}} \frac{q(1-q)}{(1+q)^3} [36 \cos 3\varphi + e(60 \cos 2\varphi + 20 \cos 4\varphi) + e^2(35 \cos \varphi + 14 \cos 3\varphi + \cos 5\varphi) + 8e^3], \quad (5)$$

$$h_{44,+}^{\text{1PN}} = \frac{\sqrt{\frac{\pi}{7}}M^3}{72da^2(1-e^2)^2} \frac{q(1-q+q^2)}{(1+q)^4} [512 \cos 4\varphi + e(1076 \cos 3\varphi + 452 \cos 5\varphi) + e^2(860 \cos 2\varphi + 568 \cos 4\varphi + 140 \cos 6\varphi) + e^3(315 \cos \varphi + 189 \cos 3\varphi + 81 \cos 5\varphi + 15 \cos 7\varphi) + 48e^4], \quad (6)$$

$$h_{44,\times}^{\text{1PN}} = -\frac{\sqrt{\frac{\pi}{7}}qM^3}{36da^2(1-e^2)^2} \frac{q(1-q+q^2)}{(1+q)^4} \sin \varphi [512(\cos \varphi + \cos 3\varphi) + e(764 + 1528 \cos 2\varphi + 452e \cos 4\varphi) + e^2(1568 \cos \varphi + 708 \cos 3\varphi + 140 \cos 5\varphi) + e^3(300 + 285 \cos 2\varphi + 96 \cos 4\varphi + 15 \cos 6\varphi)], \quad (7)$$

where M is the total mass, $q \leq 1$ is the mass ratio, a is the semi-major axis, e is the eccentricity, d is the luminosity distance to the source, and φ is the orbital phase. For each of these modes, we express the complex strain as

$$h_{lm}(t) = A_{lm}(t)e^{i\phi_{lm}(t)}, \quad (8)$$

$$A_{lm}(t) = \sqrt{(h_{lm,+})^2 + (h_{lm,\times})^2}, \quad (9)$$

$$\phi_{lm}(t) = \tan^{-1} \left(\frac{h_{lm,\times}}{h_{lm,+}} \right), \quad (10)$$

and construct the Fourier phase as

$$\Psi(t) = 2\pi ft - \phi_{lm}(t). \quad (11)$$

The general approach to solving the binary dynamics relies on the stationary-phase approximation (SPA) where one identifies t_\star such that $\dot{\Psi}(t_\star) = 0$. It turns out that, for eccentric binaries, stationary points exist, and thus the SPA holds, only for frequencies f in a bound interval $f^- \leq f \leq f^+$. In the limiting case where $f = f^\pm$, one has $\ddot{\Psi}(t_\star) = 0$, which identifies a catastrophe.

To this end, we first promote the semi-major axis a , the eccentricity e , and the orbital phase φ to functions of time, where the derivatives da/dt and de/dt are evaluated accordingly to the equations by Peters [56] while $d\varphi/dt$

is given by Kepler's law, specifically

$$\frac{da}{dt} = -\frac{64 M^3}{5 a^3} \frac{q}{(1+q)^2} \frac{(1 + \frac{73}{24}e^2 + \frac{37}{96}e^4)}{(1-e^2)^{7/2}}, \quad (12)$$

$$\frac{de}{dt} = -\frac{304 M^3}{15 a^4} \frac{q}{(1+q)^2} \frac{e(1 + \frac{121}{304}e^2)}{(1-e^2)^{5/2}}, \quad (13)$$

$$\frac{d\varphi}{dt} = \frac{M^{1/2}}{a^{3/2}} \frac{(1 + e \cos \varphi)^2}{(1 - e^2)^{3/2}}. \quad (14)$$

The frequencies at the stationary times, which we denote f_{lm} , are given by

$$f_{22}^{\text{0PN}} = \frac{\sqrt{M}}{\pi [a(1-e^2)]^{3/2}} \left\{ (1 + e \cos \varphi)^3 [8 + 12e \cos \varphi + e^2(1 + 3 \cos 2\varphi)] - \frac{M^{5/2}}{15a^{5/2}} \frac{q}{(1+q)^2} \frac{e(304 + 121e^2)}{1 - e^2} \sin \varphi \right. \\ \left. \times [4 + 8e \cos \varphi + e^2(3 + \cos 2\varphi)] \right\} [8 + 24e \cos \varphi + 13e^2(1 + \cos 2\varphi) + 2e^3(5 \cos \varphi + \cos 3\varphi) + 2e^4]^{-1} \quad (15)$$

$$f_{33}^{\text{0.5PN}} = \frac{\sqrt{M}}{\pi [a(1-e^2)]^{3/2}} \left\{ (1 + e \cos \varphi)^3 [972 + 2988e \cos \varphi + 4e^2(373 + 432 \cos 2\varphi) + e^3(897 \cos \varphi + 515 \cos 3\varphi) \right. \\ \left. + 4e^4(4 + 27 \cos 2\varphi + 15 \cos 4\varphi)] - \frac{4M^{5/2}}{15a^{5/2}} \frac{q}{(1+q)^2} \frac{e(304 + 121e^2)}{1 - e^2} \sin \varphi [90 + 288e \cos \varphi \right. \\ \left. + e^2(179 + 173 \cos 2\varphi) + 40e^3(4 \cos \varphi + \cos 3\varphi) + e^4(26 + 17 \cos 2\varphi + 3 \cos 4\varphi)] \right\} \\ \times [648 + 1880e \cos \varphi + 8e^2(313 + 321 \cos 2\varphi) + 16e^3(205 \cos \varphi + 73 \cos 3\varphi) \\ \left. + e^4(715 + 1012 \cos 2\varphi + 265 \cos 4\varphi) + 8e^5(35 \cos \varphi + 14 \cos 3\varphi + 3 \cos 5\varphi) + 32e^6]^{-1} \quad (16)$$

$$f_{44}^{\text{1PN}} = \frac{4\sqrt{M}}{\pi [a(1-e^2)]^{3/2}} \left\{ (1 + e \cos \varphi)^3 [65536 + 305664e \cos \varphi + 24e^2(11396 + 12511 \cos 2\varphi) + 4e^3(96627 \cos \varphi \right. \\ \left. + 40087 \cos 3\varphi) + 6e^4(14391 + 22594 \cos 2\varphi + 8275 \cos 4\varphi) + 3e^5(9936 \cos \varphi + 8069 \cos 3\varphi + 2835 \cos 5\varphi) \right. \\ \left. + 18e^6(8 + 89 \cos 2\varphi + 100 \cos 4\varphi + 35 \cos 6\varphi)] - \frac{8M^{5/2}}{5a^{5/2}} \frac{q}{(1+q)^2} \frac{e(304 + 121e^2)}{1 - e^2} \sin \varphi [3328 + 15360e \cos \varphi \right. \\ \left. + 8e^2(1787 + 1820 \cos 2\varphi) + 4e^3(5269 \cos \varphi + 1827 \cos 3\varphi) + 2e^4(2903 + 3942 \cos 2\varphi + 1003 \cos 4\varphi) \right. \\ \left. + 8e^5(392 \cos \varphi + 177 \cos 3\varphi + 35 \cos 5\varphi) + 3e^6(100 + 95 \cos 2\varphi + 32 \cos 4\varphi + 5 \cos 6\varphi)] \right\} \\ \times [131072 + 782336e \cos \varphi + 144e^2(6749 + 6933 \cos 2\varphi) + 32e^3(62337 \cos \varphi + 22135 \cos 3\varphi) + 8e^4(97611 \\ \left. + 135788 \cos 2\varphi + 37937 \cos 4\varphi) + 24e^5(25010 \cos \varphi + 13967 \cos 3\varphi + 3279 \cos 5\varphi) + 3e^6(23622 + 39133 \cos 2\varphi \right. \\ \left. + 18538 \cos 4\varphi + 3815 \cos 6\varphi) + 144e^7(105 \cos \varphi + 63 \cos 3\varphi + 27 \cos 5\varphi + 5 \cos 7\varphi) + 1152e^8]^{-1} \quad (17)$$

where a , φ , and e are evaluated at t_* . The leading-order terms $\propto a^{-3/2}$ arises from $d\varphi/dt$ and are thus of Newtonian order, while the next-to-leading order terms $\propto a^{-4}$ come from the adiabatic evolution of (a, e) and are suppressed by 2.5PN orders. By computing $\dot{\Psi}(t_*)$, it is straightforward to check that f_{lm} reaches a maximum/minimum at $\varphi = (0, \pi) + \mathcal{O}(M/a)^{5/2}$ which are the apocenter and the pericenter passages, respectively. We dub those frequencies f_{lm}^\pm , which are explicitly given by

$$f_{22}^\pm = \frac{2\sqrt{M}}{\pi a^{3/2}} \frac{\sqrt{1 \pm e}}{(2 \pm e)(1 \mp e)^{3/2}} + \mathcal{O} \left[\left(\frac{M}{a} \right)^5 \right], \quad (18)$$

$$f_{33}^\pm = \frac{\sqrt{M}}{2\pi a^{3/2}} \frac{27 \pm 23e}{(1 \mp e)(9 \pm 2e)\sqrt{1 - e^2}} + \mathcal{O} \left[\left(\frac{M}{a} \right)^5 \right], \quad (19)$$

$$f_{44}^\pm = \frac{\sqrt{M}}{\pi a^{3/2}} \frac{(1 \pm e)(128 \pm 87e)}{(1 \mp e)(64 \pm 63e + 6e^2)\sqrt{1 - e^2}} + \mathcal{O} \left[\left(\frac{M}{a} \right)^5 \right]. \quad (20)$$

An example is illustrated in Fig. 1. Since the frequencies f_{lm}^\pm corresponds to $\dot{\Psi}(t_*) = 0$, these signal a breakdown of the SPA and mark the presence of a catastrophe.

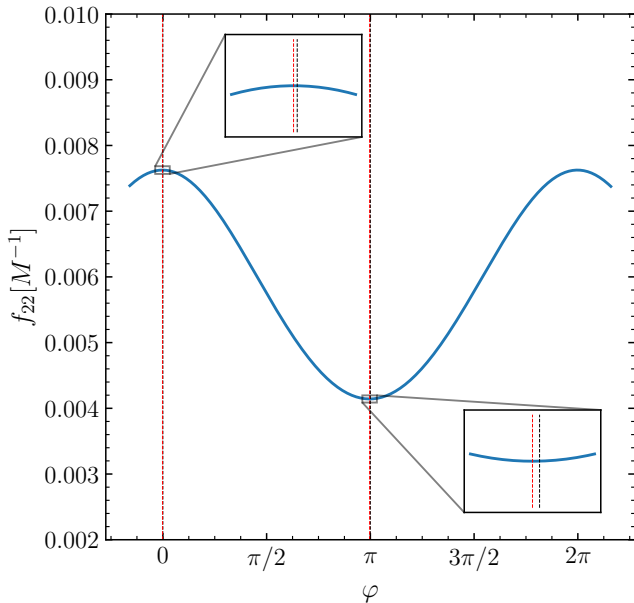


FIG. 1. Stationary frequencies of the (2,2) mode in the PN approximation. The blue curve shows the evolution of f_{22} from Eq. (15) as a function of the orbital phase φ for a system with separation $a = 15M$, eccentricity $e = 0.2$, and mass ratio $q = 1$. The two black dashed lines identify the pericenter and apocenter passage $\varphi = (0, \pi)$. The two red dashed lines indicate the extrema of f_{22} . The separation between the two sets of lines is a 2.5PN correction (see insets).

The ratio

$$\xi_{lm}(e) \equiv \frac{f_{lm}^+ - f_{lm}^-}{f_{lm}^+ + f_{lm}^-} \quad (21)$$

is a function solely of the eccentricity. From the equations above, one has

$$\xi_{22} = \frac{1}{2}e(3 - e^2) + \mathcal{O}\left[\left(\frac{M}{a}\right)^5\right], \quad (22)$$

$$\xi_{33} = \frac{396e - 46e^3}{243 + 107e^2} + \mathcal{O}\left[\left(\frac{M}{a}\right)^5\right], \quad (23)$$

$$\xi_{44} = \frac{2e(6944 - 5700e^2 + 261e^4)}{8192 - 1513e^2 - 3669e^4} + \mathcal{O}\left[\left(\frac{M}{a}\right)^5\right]. \quad (24)$$

Note that one could arrive at the above relationship between f^\pm and e simply from using solely Newtonian physics, as is evidenced by the remainder being 5PN order. While the details of the catastrophe analysis predict the saddle points to be shifted away from pericenter/apocenter by 2.5PN order corrections, i.e. $\varphi = (0, \pi) + \mathcal{O}(M/a)^{5/2}$ (see Fig. 1), the mathematical structure of Eqs. (15)-(17) conspires to force the shifts to higher PN order in Eq. (22)-(24). This should not be surprising, since adiabatic radiation reaction introduces a second, longer timescale into the two-body problem, while eccentricity is an or-

bit quantity and, thus, defined on the shorter orbital timescale.

We now invert Eqs. (22)-(24) and select the only real root in $[0, 1)$. For the (2,2) harmonic we find:

$$e_{22} = \cos(\Theta) - \sqrt{3}\sin(\Theta), \quad (25)$$

$$\Theta = \frac{1}{3} \arctan\left(\frac{\sqrt{1 - \xi_{22}^2}}{\xi_{22}}\right). \quad (26)$$

The analogous result for $(l, m) = (3, 3)$ is

$$e_{33} = \frac{1}{138} \left[-107\xi_{33} + \sqrt{54648 + 11449\xi_{33}^2} \cos(\Phi) - \sqrt{163944 + 34347\xi_{33}^2} \sin(\Phi) \right], \quad (27)$$

$$\Phi = \frac{1}{3} \arctan\left(\frac{1242\sqrt{3}}{\xi_{33}}\right) \times \frac{\sqrt{35266176 - 31184003\xi_{33}^2 - 3675129\xi_{33}^4}}{15712542 + 1225043\xi_{33}^2}. \quad (28)$$

Finally, the expression for e_{44} cannot be written down analytically because it involves solving a 5th-degree polynomial. However, it can easily be computed numerically.

The procedure we just highlighted maps the breaking points of the SPA f_{lm}^\pm to the eccentricity e where, crucially, the former can be extracted from waveform data at future null infinity and are thus gauge invariant. Our proposal is thus to promote the expressions above as a *definition* of orbital eccentricity in GR. Hereafter, we refer to these eccentricity estimates as e_c , where the subscript stands for ‘‘catastrophe.’’

B. Orbit average

For internal consistency, we apply our catastrophe analysis to the (2,2) waveforms of Eqs. (2)-(3) evolved accordingly to Eqs. (12)-(14). As an example, we select an equal mass BH binary with initial conditions $a = 15M$ and $e = 0.20$. Figure 2 shows the reconstructed evolution of e_c . In this controlled experiment, one must find $e_c = e_{\text{Newtonian}}$.

From the procedure above, estimating the eccentricity requires a value of f^+ and a value of f^- ; it can thus be performed every half orbit. One has that f^+ for the first half of the orbit is equal to f^+ for the second half of the orbit, but the former has a value of f^- that is not equal to the value of f^- of the latter. The reason is radiation reaction and simply corresponds to one’s intuition that the frequency increases as the binary inspirals toward merger.

The eccentricity estimates obtained using the evolution from apocenter to pericenter are higher than those computed using the evolution from pericenter to apocenter. We interpret these as upper and lower bounds, respectively, and assign the binary an eccentricity e_c equal to

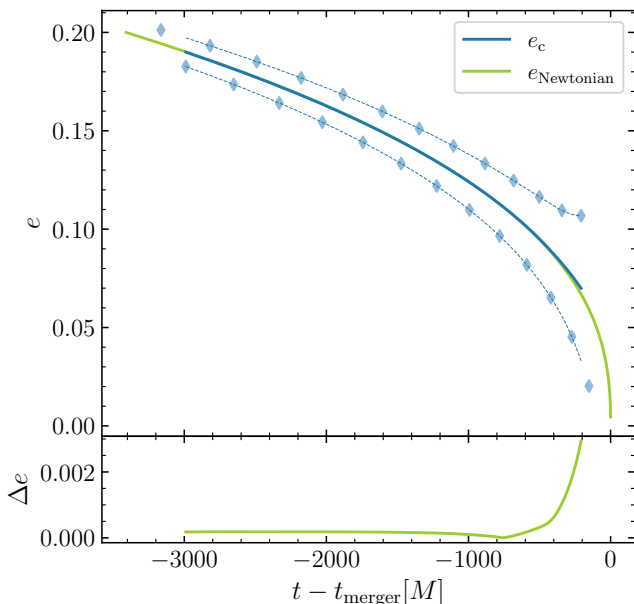


FIG. 2. Eccentricity evolution for an analytic quadrupolar waveform with mass ratio $q = 1$, initial eccentricity $e = 0.20$, and initial separation $a = 15M$. This is a controlled experiment: the top panel shows the eccentricity e_c (blue curve) predicted by our catastrophe against the assumed evolution $e_{\text{Newtonian}}$ (green curve). The former is obtained by averaging estimates from two halves of each orbit (blue diamonds and dashed curves). The bottom panel shows the absolute difference between the two predictions.

their mean. This is not an arbitrary choice but is required for internal consistency with the Newtonian limit. Indeed, the average of these two estimates is in excellent agreement with the assumed evolution up to numerical errors of $\mathcal{O}(10^{-4})$, at least up to the last few orbits before merger (amplitude maxima and minima cannot be reliably identified in that regime).

III. NUMERICAL-RELATIVITY WAVEFORMS

The procedure we just highlighted provides a practical recipe to extract the orbital eccentricity from a given gravitational waveform. Let us now look for catastrophes in full GR using NR waveforms.

A. Catastrophes in numerical relativity

As an example, we consider the eccentric BH-binary simulation SXS:BBH:1372 [38] from the SXS catalog. The simulation evolves a non-spinning, unequal-mass, eccentric binary for $t \sim 4280M$, which corresponds to ~ 17.6 orbits before merger. The following analysis uses the corresponding waveform extracted at the outermost radius with the highest available resolution.

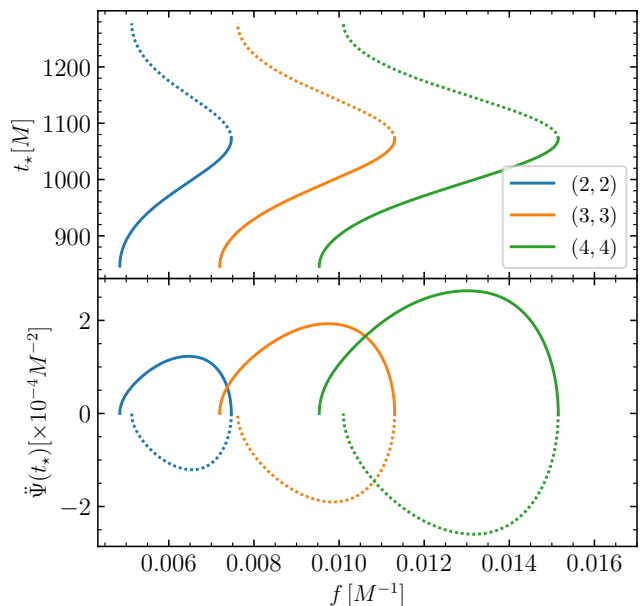


FIG. 3. Stationary point t_* (top panel) and second derivative of the Fourier phase $\ddot{\Psi}$ (bottom panel) as a function of the frequency f for a single orbit of the eccentric NR simulation SXS:BBH:1372. The halves of the orbit are indicated with solid and dotted curves. Colors indicate the different harmonic with $(l, m) = (2, 2)$ in blue, $(3, 3)$ in orange, and $(4, 4)$ in green.

We select the three harmonics $(l, m) = (2, 2)$, $(3, 3)$, $(4, 4)$, and decompose the $+$, \times polarizations into an amplitude $A_{lm}(t)$ and a phase $\phi_{lm}(t)$. We identify a single orbit using two consecutive minima (maxima) of the strain amplitude $A_{lm}(t)$ corresponding to apocenter (pericenter) passages. We compute the Fourier phase Ψ and interpolate it with splines (which are differentiable) to avoid propagating finite-difference numerical errors to $\dot{\Psi}$ and $\ddot{\Psi}$.

Figure 3 shows the stationary points t_* and the second derivative $\ddot{\Psi}$ as a function of the frequency f for each harmonic. The evolution of $\ddot{\Psi}$ describes a loop, that however does close because of radiation reaction. For each half orbit, there exists a finite region $f^- < f < f^+$ where the phase Ψ has a stationary point, while this cannot be found outside that range. The limiting case $f = f^\pm$, corresponding to a saddle point in Ψ , is a catastrophe, marking the appearance/disappearance of the stationary point itself. This is one of our key results: NR waveforms are subjected to catastrophes.

B. Weighted average

Our eccentricity estimate for simulation SXS:BBH:1372 is shown in Fig. 4. We evaluate Eqs. (25)-(28), solve numerically Eq. (24) for each half orbit, and assign to each eccentricity estimate the average time between the two orbital extrema. This procedure ensures the Newtonian limit is respected.

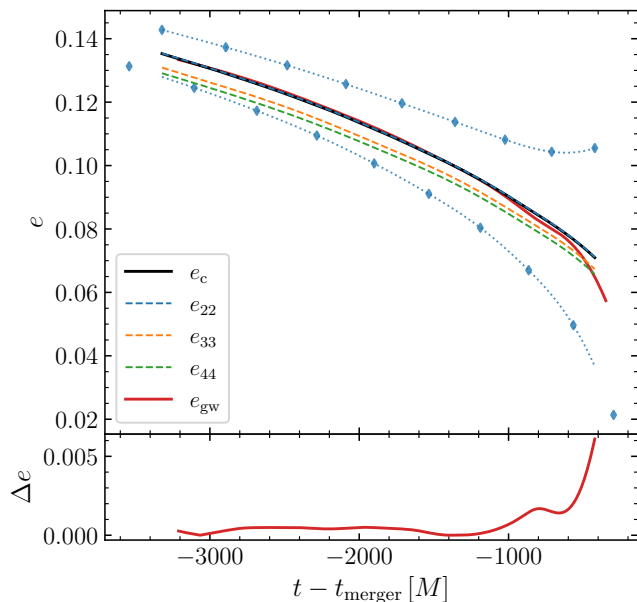


FIG. 4. Eccentricity evolution in the NR simulation SXS:BBH:1372. The blue dotted curves in the top panel show the upper (lower) bound on eccentricity estimated using half orbits from apocenter (pericenter) to pericenter (apocenter) of the (2,2) harmonic. The mean of these two curves is shown in dashed blue and corresponds to our eccentricity estimate for the (2,2) mode. The mean evolutions of the eccentricity computed from the (3,3) and (4,4) harmonics are shown in dashed orange and green, respectively. For each mode, the first and the last points are excluded to avoid extrapolation errors. The weighted average e_c is shown in solid black and almost coincides with the e_{22} estimate. The e_{gw} estimate is shown in red. For this simulation, the reference eccentricity reported in the SXS catalog is $e \simeq 0.21$ at $t - t_{\text{merger}} = -3870M$. The lower panel shows the absolute residuals between e_c and e_{gw} .

Each harmonic provides a slightly different value of the eccentricity. We suspect this is because the mapping between frequency and eccentricity derived in Sec. II makes use of the leading PN order for each mode; we leave the generalization to higher orders for future work. But these estimates should not be treated equally. They all come from the same waveform where each harmonic contributes differently. This intuition can be easily implemented with a weighted average, such that the dominant (subdominant) emission mode contributes more (less) to the final eccentricity estimate. More specifically, we consider the energy flux of each harmonic $\dot{E}_{lm} \propto |dh_{lm}/dt|^2$ [57] and weight each eccentricity contribution accordingly. Our final estimate is

$$e_c = \frac{\sum_{l,m} e_{lm} \left| \frac{dh_{lm}}{dt} \right|^2}{\sum_{l,m} \left| \frac{dh_{lm}}{dt} \right|^2} \quad (29)$$

where the sums are taken over all the modes for

which a mapping is available, in this paper $(l, m) = (2, 2), (3, 3), (4, 4)$.

For the simulation shown in Fig. 4, we find the eccentricity e_c evolves from ~ 0.14 to ~ 0.08 . These values are not compatible with the PN-based eccentricity reported in the metadata of the SXS catalog, which is ~ 0.21 at reference time $t - t_{\text{merger}} = -3870M$. The normalized weight associated with the (2,2) mode at $t - t_{\text{merger}} = -3320M$ is $\sim 97.8\%$, for the (3,3) mode is $\sim 2.1\%$, while the (4,4) mode is responsible for only 0.01% of the energy flux. This explains why e_c in Fig. 4 essentially coincides with e_{22} .

Our estimate e_c is in good agreement with the value estimate of Ref. [3], hereafter e_{gw} , which we recomputed for this simulation using their code. Residuals Δe are of $\mathcal{O}(10^{-3})$. This is not surprising because, as explored in Sec. III D, e_{gw} is equivalent to our estimator when restricted to the dominant (2,2) mode. In Fig. 4, our eccentricity evolution as a function of time is smoother than that of Ref. [3], which instead undergo small oscillations. We believe that is a spurious feature due to different implementations and numerical errors.

C. Numerical-relativity catalogs

We apply our findings to 100 NR simulations from the SXS [38] and RIT [39] groups. In particular, we select simulations with reported eccentricity $e \gtrsim 0.01$ lasting at least 7 orbits. The results of our analysis are presented in Fig. 5 using the first available estimate past junk radiation. Additional details are provided in Appendix A.

In the case of the SXS simulations, we observe discrepancies of up to 15% at eccentricities $\gtrsim 0.1$ when comparing e_c against the values reported in the catalog. Their eccentricities are estimated by fitting the orbital-frequency time derivative over the first ~ 2 orbits with a PN ansatz. In particular, we find that the majority of their values overestimates the eccentricity compared to e_c , suggesting that even the most eccentric simulations in the SXS catalog are closer to quasi-circular than what previously reported.

For the RIT simulations, their nominal eccentricity are reported assuming $e \propto r^2 d^2 r / dt^2$ where r is the coordinate separation. We find the values indicated in the RIT catalog are in better agreement with e_c , with differences of a few % and up to 10% for eccentricities $\gtrsim 0.36$.

We successfully measured the eccentricity for simulations that either do not present a catalog estimate (SXS:BBH:0324) or that only present an upper limit (SXS:BBH:1362, 1363, 1369, 1370, 1374). For a particular case (SXS:BBH:0147), the combination of significant spin precession and too-short signal makes our current implementation inconclusive because amplitude peaks cannot be confidently identified. We can compute eccentricities in several cases for which the e_{gw} code cannot provide an estimate (SXS:BBH:0078, 0082, 0088, 0094, 0097, 0098, 0179, 1149, 1160, 1169, 1366, 1371, 1373, 1388). This is due to code implementation, which returns an error

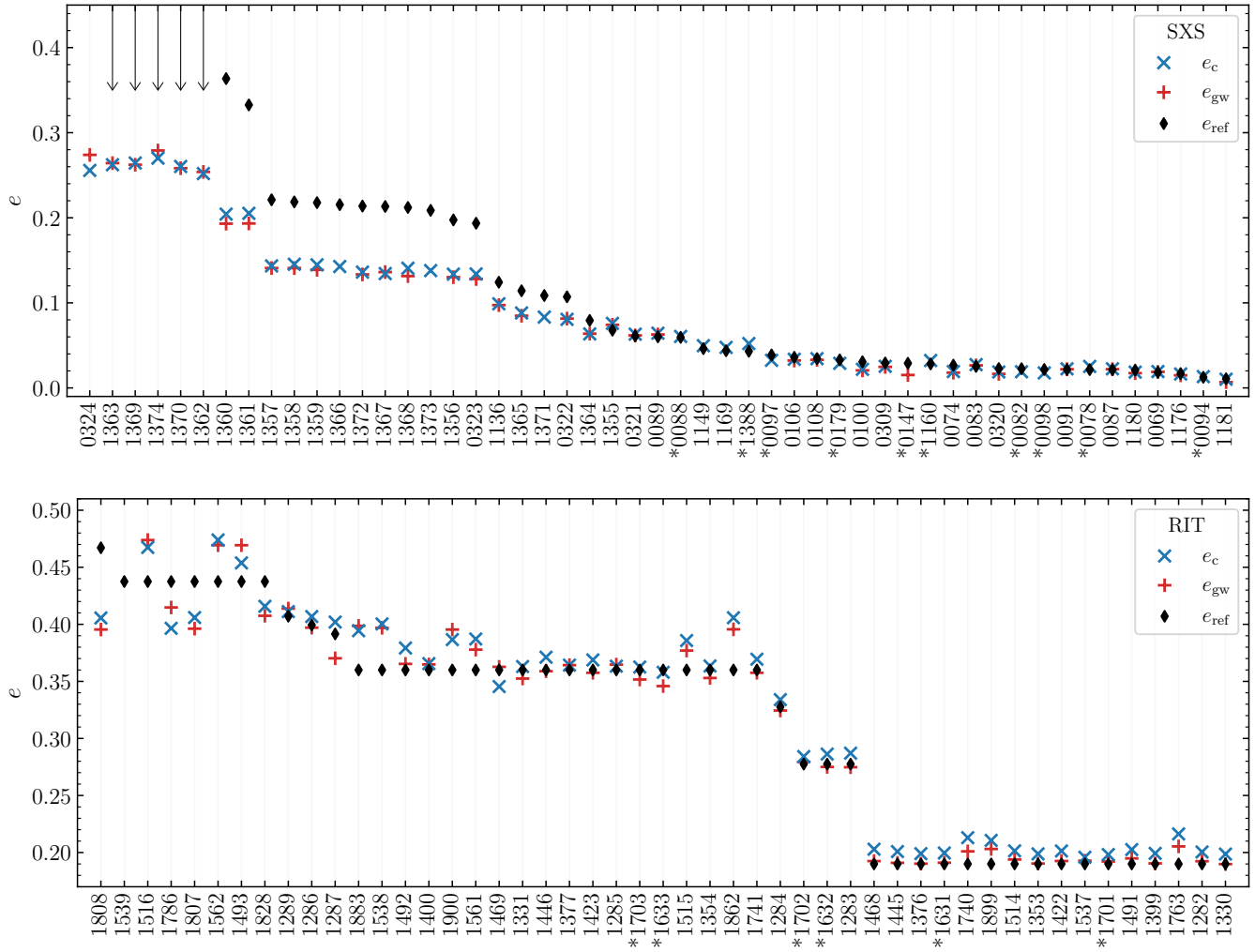


FIG. 5. Eccentric NR catalogs. The top (bottom) panel shows eccentricity estimates for the most eccentric simulations in the SXS [38] (RIT [39]) catalog. Black diamonds indicate the nominal eccentricity value reported in the catalog at the reference time. In a few cases, this estimate is provided as an upper limit (down-pointing arrows) and in a few others is not provided at all. Blue crosses refer to our e_c estimates measured at the earliest possible time past junk radiation. Similarly, red markers indicate e_{gw} from Ref. [3]. Stars next to the ID numbers on the x -axis identify simulations with precessing effective spin $\chi_p > 0.01$.

for highly precessing systems, and not to the definition itself. For the RIT runs, the simulations with the largest discrepancies (RIT:eBBH:1539, 1808, 1862) correspond to the shorter waveforms. Shorter waveforms correspond to more rapidly evolving binaries that are closer to merger and it is more difficult to extract eccentricity from these. All methods struggle in this regime.

There is an important caveat in this comparison, which is related to the time, or frequency, at which the eccentricity is measured. NR catalogs report the value of e at some reference time past junk radiation, and this depends on the length of the simulations themselves. Estimating e_c require at least one pericenter and one apocenter passage (which are identified from the waveform), resulting in an eccentricity measure at some marginally larger time. This time difference mostly affects the analysis of highly eccentric and short waveforms, where the eccentricity evolves

faster. This partially, but not fully, mitigates the reported differences. The times of eccentricity measurements are reported in Appendix A.

D. Comparison with e_{gw}

Overall, we find that the eccentricity e_c we extract from NR waveforms disagrees with the nominal values reported in the catalogs but largely agrees with e_{gw} from Refs. [3, 40], which we report here for completeness:

$$e_{\text{gw}} = \cos(\psi/3) - \sqrt{3} \sin(\psi/3), \quad (30)$$

$$\psi = \arctan\left(\frac{1 - e_{\omega_{22}}^2}{2e_{\omega_{22}}}\right), \quad (31)$$

$$e_{\omega_{22}} = \frac{\sqrt{\omega_{22}^p(t)} - \sqrt{\omega_{22}^a(t)}}{\sqrt{\omega_{22}^p(t)} + \sqrt{\omega_{22}^a(t)}}. \quad (32)$$

Indeed, some non-trivial algebraic manipulation shows that the (2,2) mode estimate presented in Eqs. (25)-(26) is formally equivalent to the expression above. The median of the absolute difference between the two definitions across the two sets of simulations is $\sim 6.5 \times 10^{-3}$, and we report that they differ by more than 1% in $\sim 8\%$ ($\sim 39\%$) of the cases among the SXS (RIT) simulations considered in this analysis. The larger discrepancies occurring in the second set are mostly due to different measuring times (see Appendix A).

We stress that the derivations of e_c and e_{gw} are different, with the former relying on the breakdown of the SPA and the latter relying on the instantaneous GW phase. In particular, the construction of e_{gw} requires adjustments to ensure the resulting eccentricity estimator has the correct Newtonian limit. On the other hand, this is automatically implemented in our procedure, which makes explicit use of the said limit to derive the mapping between the catastrophe frequencies and the eccentricity. Our estimator e_c includes emission modes of higher order, unlike e_{gw} which was explicitly restricted to the dominant harmonic. That said, the (2,2) mode is the most important contribution entering the weighted average of Eq. (29).

IV. CONCLUSIONS

Catastrophe theory provides an ideal framework to define the orbital eccentricity in GR. Measuring e_c relies solely on the gravitational waveform and is thus fully gauge invariant. The Newtonian limit is also naturally built into the definition itself.

The eccentricity definition we put forward is fully generic; the only limitation is the resolution of the underlying NR simulations as one needs to confidently identify peaks in the waveform amplitude. At present, this limits the applicability of our analysis to values $e_c \gtrsim 0.01$ (but note that eccentricities smaller than this threshold are unlikely to be distinguished from zero with current GW detectors [58]). We stress that this limitation is related only to the implementation and to the extremization rou-

tine, not to the theoretical foundations of this technique. On the contrary, at very high eccentricity ($e \gtrsim 0.6$), the orbit-averaged approach [56] entering the mapping via Eqs. (12)-(13) is no longer valid [24, 59]. This is due to the derivation strategy pursued in this paper and does not limit the applicability of catastrophe theory to eccentric BH binaries.

In this paper, the $f_{\pm} \rightarrow e$ mapping is modeled using the $(l, m) = (2, 2)$, $(3, 3)$ and $(4, 4)$ harmonics at their leading PN order. Our approach is generic and can be generalized to other modes using the appropriate PN expressions. This will be increasingly relevant for large values of the eccentricity because power leaks into higher and higher harmonics [60].

Extracting e_c only requires the waveform time series and can thus be applied to GW signals detected with current and future interferometers. In the short term, we envision this as a post-processing exercise on high-level GW data, namely posterior samples. As such, using e_c does not require changing the eccentricity definition internally employed by waveform approximants. This contributes to current attempts aimed at properly comparing the notions of eccentricity used in astrophysical models and those used in GW data analysis [61–63]. In the long run, e_c estimates might be exploited when building new waveform approximants, thus contributing to making models closer to the physical, gauge-invariant observables.

ACKNOWLEDGMENTS

We thank Md Arif Shaikh, Harald Pfeiffer, Vijay Varma, Antoni Ramos Buades, Enrico Barausse, Costantino Pacilio, and Bruno Giacomazzo for discussions. M.B., N.L, D.G., and G.F are supported by ERC Starting Grant No. 945155–GWmining, Cariplo Foundation Grant No. 2021-0555, MUR PRIN Grant No. 2022-Z9X4XS, MUR Grant “Progetto Dipartimenti di Eccellenza 2023-2027” (BiCoQ), and the ICSC National Research Centre funded by NextGenerationEU. D.G. is supported by MSCA Fellowships No. 101064542–StochRewind and No. 101149270–ProtoBH. Computational work was performed at CINECA with allocations through INFN and Bicocca.

-
- [1] N. Loutrel, S. Liebersbach, N. Yunes, and N. Cornish, *Class. Quantum Grav.* **36**, 025004 (2019), [arXiv:1810.03521 \[gr-qc\]](#).
 - [2] L. Blanchet, *Living Rev. Rel.* **17**, 2 (2014), [arXiv:1310.1528 \[gr-qc\]](#).
 - [3] M. A. Shaikh, V. Varma, H. P. Pfeiffer, A. Ramos-Buades, and M. van de Meent, *Phys. Rev. D* **108**, 104007 (2023), [arXiv:2302.11257 \[gr-qc\]](#).
 - [4] B. P. Abbott *et al.*, *Phys. Rev. X* **9**, 031040 (2019), [arXiv:1811.12907 \[astro-ph.HE\]](#).
 - [5] R. Abbott *et al.*, *Phys. Rev. X* **11**, 021053 (2021), [arXiv:2010.14527 \[gr-qc\]](#).
 - [6] R. Abbott *et al.*, *Phys. Rev. D* **109**, 022001 (2024), [arXiv:2108.01045 \[gr-qc\]](#).
 - [7] R. Abbott *et al.*, *Phys. Rev. X* **13**, 041039 (2023), [arXiv:2111.03606 \[gr-qc\]](#).
 - [8] M. Maggiore *et al.*, *J. Cosmology Astropart. Phys.* **2020**, 050 (2020), [arXiv:1912.02622 \[astro-ph.CO\]](#).
 - [9] D. Reitze *et al.*, in *Bull. Am. Astron. Soc.*, Vol. 51 (2019) p. 35, [arXiv:1907.04833 \[astro-ph.IM\]](#).

- [10] M. Mapelli, in *Handbook of Gravitational Wave Astronomy* (Springer Singapore, 2021) p. 16.
- [11] I. Mandel and A. Farmer, *Phys. Rep.* **955**, 1 (2022), arXiv:1806.05820 [astro-ph.HE].
- [12] M. Colpi *et al.*, (2024), arXiv:2402.07571 [astro-ph.CO].
- [13] E. Barausse and A. Lapi, in *Handbook of Gravitational Wave Astronomy* (Springer Singapore, 2021) p. 18.
- [14] M. Volonteri, M. Habouzit, and M. Colpi, *Nat. Rev. Phys.* **3**, 732 (2021), arXiv:2110.10175 [astro-ph.GA].
- [15] I. Romero-Shaw, P. D. Lasky, and E. Thrane, *Astrophys. J.* **940**, 171 (2022), arXiv:2206.14695 [astro-ph.HE].
- [16] N. Gupte, A. Ramos-Buades, A. Buonanno, J. Gair, M. C. Miller, M. Dax, S. R. Green, M. Pürrer, J. Wildberger, J. Macke, and B. Schölkopf, (2024), arXiv:2404.14286 [gr-qc].
- [17] H. L. Iglesias, J. Lange, I. Bartos, S. Bhaumik, R. Gamba, V. Gayathri, A. Jan, R. Nowicki, R. O'Shaughnessy, D. M. Shoemaker, R. Venkataramanan, and K. Wagner, *Astrophys. J.* **972**, 65 (2024), arXiv:2208.01766 [gr-qc].
- [18] G. Fumagalli, I. Romero-Shaw, D. Gerosa, V. De Renzi, K. Kritos, and A. Olejak, (2024), arXiv:2405.14945 [astro-ph.HE].
- [19] P. Saini, S. A. Bhat, M. Favata, and K. G. Arun, *Phys. Rev. D* **109**, 084056 (2024), arXiv:2311.08033 [gr-qc].
- [20] A. Gupta, *et al.*, (2024), arXiv:2405.02197 [gr-qc].
- [21] S. Tanay, M. Haney, and A. Gopakumar, *Phys. Rev. D* **93**, 064031 (2016), arXiv:1602.03081 [gr-qc].
- [22] M. van de Meent and N. Warburton, *Class. Quantum Grav.* **35**, 144003 (2018), arXiv:1802.05281 [gr-qc].
- [23] B. Moore, T. Robson, N. Loutrel, and N. Yunes, *Class. Quantum Grav.* **35**, 235006 (2018), arXiv:1807.07163 [gr-qc].
- [24] B. Moore and N. Yunes, *Class. Quantum Grav.* **36**, 185003 (2019), arXiv:1903.05203 [gr-qc].
- [25] N. Loutrel, *Class. Quantum Grav.* **37**, 075008 (2020), arXiv:1909.02143 [gr-qc].
- [26] A. Nagar, P. Rettegno, R. Gamba, and S. Bernuzzi, *Phys. Rev. D* **103**, 064013 (2021), arXiv:2009.12857 [gr-qc].
- [27] T. Islam, V. Varma, J. Lodman, S. E. Field, G. Khanna, M. A. Scheel, H. P. Pfeiffer, D. Gerosa, and L. E. Kidder, *Phys. Rev. D* **103**, 064022 (2021), arXiv:2101.11798 [gr-qc].
- [28] S. A. Hughes, N. Warburton, G. Khanna, A. J. K. Chua, and M. L. Katz, *Phys. Rev. D* **103**, 104014 (2021), arXiv:2102.02713 [gr-qc].
- [29] M. L. Katz, A. J. K. Chua, L. Speri, N. Warburton, and S. A. Hughes, *Phys. Rev. D* **104**, 064047 (2021), arXiv:2104.04582 [gr-qc].
- [30] X. Liu, Z. Cao, and Z.-H. Zhu, *Class. Quantum Grav.* **39**, 035009 (2022), arXiv:2102.08614 [gr-qc].
- [31] A. Ramos-Buades, A. Buonanno, M. Khalil, and S. Ossokine, *Phys. Rev. D* **105**, 044035 (2022), arXiv:2112.06952 [gr-qc].
- [32] G. Cho, S. Tanay, A. Gopakumar, and H. M. Lee, *Phys. Rev. D* **105**, 064010 (2022), arXiv:2110.09608 [gr-qc].
- [33] P. Lynch, M. van de Meent, and N. Warburton, *Class. Quantum Grav.* **39**, 145004 (2022), arXiv:2112.05651 [gr-qc].
- [34] A. Nagar, R. Gamba, P. Rettegno, V. Fantini, and S. Bernuzzi, *Phys. Rev. D* **110**, 084001 (2024), arXiv:2404.05288 [gr-qc].
- [35] J. N. Arredondo, A. Klein, and N. Yunes, *Phys. Rev. D* **110**, 044044 (2024), arXiv:2402.06804 [gr-qc].
- [36] R. Gamba, D. Chiaramello, and S. Neogi, *Phys. Rev. D* **110**, 024031 (2024), arXiv:2404.15408 [gr-qc].
- [37] E. A. Huerta, R. Haas, S. Habib, A. Gupta, A. Rebei, V. Chavva, D. Johnson, S. Rosofsky, E. Wessel, B. Agarwal, D. Luo, and W. Ren, *Phys. Rev. D* **100**, 064003 (2019), arXiv:1901.07038 [gr-qc].
- [38] M. Boyle *et al.*, *Class. Quantum Grav.* **36**, 195006 (2019), arXiv:1904.04831 [gr-qc].
- [39] J. Healy and C. O. Lousto, *Phys. Rev. D* **105**, 124010 (2022), arXiv:2202.00018 [gr-qc].
- [40] A. Ramos-Buades, M. van de Meent, H. P. Pfeiffer, H. R. Rüter, M. A. Scheel, M. Boyle, and L. E. Kidder, *Phys. Rev. D* **106**, 124040 (2022), arXiv:2209.03390 [gr-qc].
- [41] D. Ferguson *et al.*, (2023), arXiv:2309.00262 [gr-qc].
- [42] G. Ficarra and C. O. Lousto, (2024), arXiv:2409.18728 [gr-qc].
- [43] A. H. Mroue *et al.*, *Phys. Rev. Lett.* **111**, 241104 (2013), arXiv:1304.6077 [gr-qc].
- [44] A. Buonanno, L. E. Kidder, A. H. Mroué, H. P. Pfeiffer, and A. Taracchini, *Phys. Rev. D* **83**, 104034 (2011), arXiv:1012.1549 [gr-qc].
- [45] A. Ramos-Buades, S. Husa, and G. Pratten, *Phys. Rev. D* **99**, 023003 (2019), arXiv:1810.00036 [gr-qc].
- [46] R. Thom, *Structural stability and morphogenesis - an outline of a general theory of models*, Advanced book classics (Addison-Wesley, 1989).
- [47] M. Golubitsky, *SIAM Review* **20**, 352 (1978).
- [48] P. T. Saunders, *An Introduction to Catastrophe Theory* (Cambridge University Press, 1980).
- [49] E. C. Zeeman, *Scientific American* **234**, 65 (1976).
- [50] P. Roopnarine, in *Encyclopedia of Ecology* (Academic Press, Oxford, 2008) pp. 531–536.
- [51] I. Stewart, *Phys. D: Nonlinear Phenom.* **2**, 245 (1981).
- [52] J. A. Adam, *Phys. Rep.* **356**, 229 (2002).
- [53] N. Loutrel, *Class. Quantum Grav.* **40**, 215004 (2023), arXiv:2304.00836 [gr-qc].
- [54] T. Damour and N. Deruelle, *Ann. Inst. H. Poincaré Phys. Théor.* **43**, 107 (1985).
- [55] E. Poisson and C. M. Will, *Gravity: Newtonian, Post-Newtonian, Relativistic* (Cambridge University Press, 2014).
- [56] P. C. Peters, *Phys. Rev.* **136**, 1224 (1964).
- [57] M. Ruiz, M. Alcubierre, D. Núñez, and R. Takahashi, *Gen. Relat. Gravit.* **40**, 1705 (2008), arXiv:0707.4654 [gr-qc].
- [58] M. E. Lower, E. Thrane, P. D. Lasky, and R. Smith, *Phys. Rev. D* **98**, 083028 (2018), arXiv:1806.05350 [astro-ph.HE].
- [59] G. Fumagalli and D. Gerosa, *Phys. Rev. D* **108**, 124055 (2023), arXiv:2310.16893 [gr-qc].
- [60] P. C. Peters and J. Mathews, *Phys. Rev.* **131**, 435 (1963).
- [61] A. Bonino, R. Gamba, P. Schmidt, A. Nagar, G. Pratten, M. Breschi, P. Rettegno, and S. Bernuzzi, *Phys. Rev. D* **107**, 064024 (2023), arXiv:2207.10474 [gr-qc].
- [62] A. Bonino, P. Schmidt, and G. Pratten, (2024), arXiv:2404.18875 [gr-qc].
- [63] A. Vijaykumar, A. G. Hanselman, and M. Zevin, *Astrophys. J.* **969**, 132 (2024), arXiv:2402.07892 [astro-ph.HE].

Appendix A: Properties of the NR simulations

We provide details on the NR simulations analyzed in this paper. Table II reports the mass ratio q , the effective spin χ_{eff} , the precessing parameter χ_p , and the number of orbits n_{orb} . For each simulation, we list the nominal eccentricity e_{ref} provided in the catalog metadata, which is measured at time t_{ref} . The estimates e_{22} , e_{33} , e_{44} are evaluated at earliest possible times past junk radiation. The e_c values refer to the first common time at which the eccentricities for the three harmonics are defined t_c . For e_{gw} , we use the code of Ref. [3] selecting their ‘‘amplitude’’ method flag, the estimates e_{gw} are measured at the earliest time t_{gw} as defined in their code.

	q	χ_{eff}	χ_p	n_{orb}	e_{ref}	$t_{\text{ref}}[M]$	e_{22}	e_{33}	e_{44}	e_c	$t_c[M]$	e_{gw}	$t_{\text{gw}}[M]$
SXS:BBH:0324	0.82	-1.7×10^{-2}	2.1×10^{-8}	13.04	—	-2790	0.256	0.260	0.301	0.256	-2148	0.274	-2052
SXS:BBH:1363	1.00	3.5×10^{-6}	5.3×10^{-8}	12.18	< 1.80	-2509	0.262	—	0.292	0.262	-1884	0.264	-1773
SXS:BBH:1369	0.50	4.4×10^{-5}	5.1×10^{-8}	13.92	< 1.80	-2895	0.265	0.281	0.329	0.264	-2346	0.262	-2254
SXS:BBH:1374	0.33	-6.5×10^{-5}	1.3×10^{-7}	15.59	< 1.70	-3413	0.270	0.277	0.275	0.270	-2975	0.279	-2644
SXS:BBH:1370	0.50	2.8×10^{-5}	9.2×10^{-8}	13.23	< 1.70	-2649	0.260	0.266	0.269	0.260	-2148	0.258	-2038
SXS:BBH:1362	1.00	1.2×10^{-5}	2.0×10^{-8}	12.28	< 1.70	-2567	0.252	—	0.422	0.252	-1709	0.254	-1812
SXS:BBH:1360	1.00	-4.5×10^{-7}	7.0×10^{-9}	13.14	0.364	-2791	0.204	—	0.199	0.204	-2363	0.193	-2043
SXS:BBH:1361	1.00	-6.5×10^{-6}	4.2×10^{-8}	12.98	0.333	-2713	0.205	—	0.204	0.205	-2316	0.193	-2003
SXS:BBH:1357	1.00	-1.9×10^{-5}	2.3×10^{-8}	14.76	0.221	-3284	0.143	—	0.138	0.143	-2647	0.141	-2537
SXS:BBH:1358	1.00	-2.6×10^{-5}	6.6×10^{-8}	14.08	0.219	-3056	0.145	—	0.140	0.145	-2643	0.141	-2324
SXS:BBH:1359	1.00	-1.5×10^{-5}	3.7×10^{-9}	13.75	0.218	-2948	0.145	—	0.139	0.145	-2527	0.139	-2211
SXS:BBH:1366	0.50	1.2×10^{-4}	3.1×10^{-6}	15.62	0.215	-3477	0.143	0.144	0.136	0.143	-3053	—	—
SXS:BBH:1372	0.33	3.1×10^{-5}	2.4×10^{-7}	17.66	0.214	-3870	0.136	0.137	0.130	0.136	-3320	0.133	-3210
SXS:BBH:1367	0.50	-4.0×10^{-5}	9.1×10^{-8}	15.31	0.213	-3027	0.134	0.135	0.128	0.134	-2513	0.136	-2618
SXS:BBH:1368	0.50	-7.7×10^{-5}	9.9×10^{-8}	15.03	0.212	-3259	0.141	0.142	0.135	0.141	-2842	0.131	-2522
SXS:BBH:1373	0.33	2.1×10^{-5}	9.1×10^{-8}	17.31	0.209	-3785	0.138	0.139	0.132	0.138	-3432	—	—
SXS:BBH:1356	1.00	2.4×10^{-6}	2.9×10^{-8}	22.34	0.197	-6448	0.134	—	0.129	0.134	-5862	0.130	-5455
SXS:BBH:0323	0.82	-1.7×10^{-2}	7.6×10^{-8}	14.63	0.194	-3212	0.134	0.135	0.128	0.134	-2806	0.128	-2485
SXS:BBH:1136	1.00	-7.5×10^{-1}	5.1×10^{-8}	9.51	0.124	-1820	0.099	—	0.093	0.099	-1453	0.097	-1352
SXS:BBH:1365	0.50	2.3×10^{-5}	4.1×10^{-7}	16.06	0.114	-3554	0.088	0.088	0.085	0.088	-3180	0.085	-2853
SXS:BBH:1371	0.33	4.1×10^{-5}	2.2×10^{-7}	18.17	0.109	-4102	0.083	0.083	0.080	0.083	-3699	—	—
SXS:BBH:0322	0.82	-1.7×10^{-2}	4.6×10^{-8}	14.97	0.107	-2990	0.081	0.080	0.077	0.081	-2499	0.081	-2604
SXS:BBH:1364	0.50	2.0×10^{-5}	2.8×10^{-7}	16.14	0.079	-3272	0.063	0.063	0.061	0.063	-2785	0.064	-2889
SXS:BBH:1355	1.00	-1.6×10^{-5}	2.5×10^{-8}	13.90	0.068	-2936	0.076	—	0.072	0.076	-2452	0.074	-2347
SXS:BBH:0321	0.82	-1.7×10^{-2}	1.4×10^{-7}	14.98	0.061	-3305	0.063	0.062	0.060	0.063	-2761	0.062	-2653
SXS:BBH:0089	1.00	-2.5×10^{-1}	2.3×10^{-10}	31.06	0.060	-11363	0.064	—	0.063	0.064	-10662	0.063	-10154
SXS:BBH:0088	1.00	1.2×10^{-5}	5.0×10^{-1}	31.87	0.059	-11285	0.061	—	0.060	0.061	-10560	—	—
SXS:BBH:1149	0.33	6.8×10^{-1}	7.7×10^{-7}	24.10	0.046	-5169	0.050	0.049	0.048	0.050	-4753	—	—
SXS:BBH:1169	0.33	-6.7×10^{-1}	2.7×10^{-6}	22.07	0.044	-6426	0.048	0.047	0.046	0.048	-5729	—	—
SXS:BBH:1388	0.33	4.2×10^{-1}	5.8×10^{-1}	23.60	0.043	-5330	0.052	0.046	0.047	0.052	-4942	—	—
SXS:BBH:0097	0.67	1.3×10^{-4}	5.0×10^{-1}	19.24	0.039	-5074	0.032	0.039	0.033	0.032	-4386	—	—
SXS:BBH:0106	0.20	1.9×10^{-7}	4.9×10^{-10}	21.32	0.036	-4669	0.034	0.033	0.032	0.034	-4306	0.032	-3980
SXS:BBH:0108	0.20	-4.2×10^{-1}	6.2×10^{-11}	20.73	0.034	-5226	0.034	0.034	0.033	0.034	-4703	0.033	-4333
SXS:BBH:0179	0.67	6.5×10^{-1}	8.7×10^{-2}	23.75	0.033	-5714	0.029	0.030	0.028	0.029	-5368	—	—
SXS:BBH:0100	0.67	1.2×10^{-7}	7.3×10^{-10}	27.36	0.031	-8472	0.022	0.021	0.021	0.022	-7969	0.021	-7526
SXS:BBH:0309	0.82	-1.6×10^{-2}	1.2×10^{-7}	15.75	0.029	-3258	0.025	0.024	0.024	0.025	-2806	0.025	-2906
SXS:BBH:0147	1.00	-1.1×10^{-3}	5.0×10^{-1}	7.12	0.029	-882	—	—	—	—	—	0.015	-510
SXS:BBH:1160	0.33	2.2×10^{-1}	5.9×10^{-1}	22.36	0.028	-4901	0.032	0.033	0.032	0.032	-4489	—	—
SXS:BBH:0074	1.00	1.3×10^{-7}	1.2×10^{-9}	26.23	0.027	-8037	0.019	—	0.018	0.019	-7548	0.018	-7105
SXS:BBH:0083	1.00	2.5×10^{-1}	2.8×10^{-9}	32.40	0.025	-11067	0.027	—	0.027	0.027	-10491	0.027	-9715
SXS:BBH:0320	0.82	-1.7×10^{-2}	1.0×10^{-7}	13.49	0.023	-2447	0.019	0.018	0.018	0.019	-1981	0.017	-2067
SXS:BBH:0082	0.67	7.8×10^{-4}	5.0×10^{-1}	19.77	0.023	-5310	0.019	0.025	0.018	0.019	-4588	—	—
SXS:BBH:0098	0.67	6.9×10^{-4}	5.0×10^{-1}	27.53	0.022	-8614	0.018	0.025	0.017	0.018	-8032	—	—
SXS:BBH:0091	1.00	9.8×10^{-8}	2.2×10^{-9}	34.18	0.022	-12498	0.022	—	0.022	0.022	-11647	0.022	-11154
SXS:BBH:0078	0.67	7.9×10^{-4}	5.0×10^{-1}	23.21	0.022	-6811	0.025	0.016	0.024	0.025	-6281	—	—
SXS:BBH:0087	1.00	1.2×10^{-7}	1.4×10^{-9}	29.96	0.021	-10161	0.022	—	0.023	0.022	-9387	0.022	-8924
SXS:BBH:1180	0.33	-1.1×10^{-4}	3.2×10^{-7}	15.34	0.021	-2781	0.019	0.018	0.018	0.019	-2389	0.017	-2476

	q	χ_{eff}	χ_p	n_{orb}	e_{ref}	$t_{\text{ref}}[M]$	e_{22}	e_{33}	e_{44}	e_c	$t_c[M]$	e_{gw}	$t_{\text{gw}}[M]$
SXS:BBH:0069	1.00	1.2×10^{-7}	1.6×10^{-9}	30.07	0.018	-10245	0.019	—	0.019	0.019	-9476	0.019	-9010
SXS:BBH:1176	0.33	-4.7×10^{-6}	1.3×10^{-7}	15.69	0.017	-2900	0.016	0.016	0.015	0.016	-2512	0.015	-2594
SXS:BBH:0094	0.67	3.5×10^{-4}	5.0×10^{-1}	21.42	0.013	-5993	0.014	0.018	0.015	0.013	-5369	—	—
SXS:BBH:1181	0.33	2.1×10^{-5}	9.5×10^{-8}	15.13	0.011	-2884	0.010	0.010	0.010	0.010	-2667	0.007	-2339
RIT:eBBH:1808	1.00	8.0×10^{-1}	0	11.75	0.467	-2291	0.406	—	0.440	0.406	-1363	0.395	-1251
RIT:eBBH:1539	0.17	3.8×10^{-6}	0	9.89	0.438	-2154	0.520	0.510	0.539	0.520	-1301	0.517	-1412
RIT:eBBH:1516	0.20	0	0	11.34	0.438	-2436	0.468	0.467	0.452	0.467	-1615	0.474	-1724
RIT:eBBH:1786	1.00	5.0×10^{-1}	0	11.37	0.438	-2390	0.398	—	0.395	0.397	-1391	0.415	-1707
RIT:eBBH:1807	1.00	8.0×10^{-1}	0	13.83	0.438	-2924	0.408	—	0.434	0.406	-2115	0.396	-2023
RIT:eBBH:1562	0.14	0	0	12.31	0.438	-2621	0.475	0.471	0.457	0.474	-1791	0.469	-1688
RIT:eBBH:1493	0.25	0	0	9.64	0.438	-2044	0.454	0.452	0.439	0.454	-1244	0.469	-1688
RIT:eBBH:1828	1.00	4.0×10^{-1}	0	10.54	0.438	-2216	0.418	—	0.403	0.416	-1434	0.407	-1332
RIT:eBBH:1289	1.00	0	0	9.36	0.407	-2083	0.411	—	0.413	0.411	-1273	0.414	-1373
RIT:eBBH:1286	1.00	0	0	10.07	0.399	-2272	0.407	—	0.408	0.407	-1448	0.397	-1331
RIT:eBBH:1287	1.00	0	0	10.49	0.392	-2449	0.402	—	0.397	0.402	-1615	0.370	-1270
RIT:eBBH:1883	0.50	-2.7×10^{-1}	0	8.96	0.360	-2200	0.394	0.391	0.390	0.394	-1307	0.399	-1421
RIT:eBBH:1538	0.17	0	0	12.94	0.360	-3140	0.400	0.405	0.385	0.400	-2005	0.397	-2103
RIT:eBBH:1492	0.25	0	0	18.31	0.360	-4820	0.379	0.378	0.378	0.379	-3657	0.365	-3498
RIT:eBBH:1400	0.60	0	0	13.91	0.360	-3539	0.366	0.365	0.354	0.366	-2403	0.365	-2509
RIT:eBBH:1900	1.00	-4.0×10^{-1}	0	9.69	0.360	-2426	0.388	—	0.398	0.387	-1530	0.395	-1913
RIT:eBBH:1561	0.14	0	0	23.84	0.360	-6431	0.387	0.392	0.389	0.387	-5252	0.378	-5359
RIT:eBBH:1469	0.33	0	0	16.09	0.360	-4191	0.376	0.373	0.368	0.345	-2233	0.363	-2889
RIT:eBBH:1331	0.90	0	0	13.35	0.360	-3364	0.363	0.362	0.351	0.363	-2233	0.352	-2093
RIT:eBBH:1446	0.40	0	0	15.42	0.360	-3942	0.371	0.369	0.364	0.371	-2796	0.359	-2647
RIT:eBBH:1377	0.70	0	0	13.38	0.360	-3440	0.364	0.363	0.354	0.364	-2306	0.364	-2412
RIT:eBBH:1423	0.50	0	0	14.46	0.360	-3657	0.369	0.367	0.360	0.369	-2519	0.358	-2374
RIT:eBBH:1285	1.00	0	0	13.02	0.360	-3310	0.364	—	0.357	0.363	-2172	0.365	-2288
RIT:eBBH:1703	1.00	0	7.0×10^{-1}	13.02	0.360	-3324	0.363	—	0.344	0.363	-2195	0.352	-2063
RIT:eBBH:1633	1.00	0	7.0×10^{-1}	13.40	0.360	-3433	0.358	—	0.344	0.358	-2296	0.346	-2163
RIT:eBBH:1515	0.20	2.0×10^{-6}	0	20.65	0.360	-5480	0.386	0.389	0.379	0.386	-4302	0.377	-4409
RIT:eBBH:1354	0.80	0	0	13.22	0.360	-3388	0.364	0.362	0.351	0.364	-2256	0.353	-2116
RIT:eBBH:1862	0.33	-2.0×10^{-1}	0	8.51	0.360	-2151	0.407	0.404	0.394	0.406	-1235	0.396	-1133
RIT:eBBH:1741	1.00	-5.0×10^{-1}	0	9.12	0.360	-2229	0.370	—	0.354	0.369	-1109	0.358	-2374
RIT:eBBH:1284	1.00	0	0	15.84	0.328	-4372	0.334	—	0.325	0.334	-3164	0.324	-3020
RIT:eBBH:1702	1.00	0	7.0×10^{-1}	20.98	0.278	-6496	0.284	—	0.290	0.284	-5183	0.279	-5028
RIT:eBBH:1632	1.00	0	7.0×10^{-1}	21.50	0.278	-6666	0.286	—	0.297	0.286	-5349	0.275	-4928
RIT:eBBH:1283	1.00	0	0	20.93	0.278	-6466	0.287	—	0.287	0.287	-5153	0.275	-4732
RIT:eBBH:1468	0.33	0	0	40.24	0.190	-15055	0.203	0.219	0.223	0.203	-13568	0.193	-13696
RIT:eBBH:1445	0.40	0	0	38.11	0.190	-14182	0.201	0.217	0.221	0.201	-12695	0.191	-12823
RIT:eBBH:1376	0.70	0	0	33.12	0.190	-12234	0.199	0.216	0.219	0.199	-10752	0.190	-10554
RIT:eBBH:1631	1.00	0	7.0×10^{-1}	32.31	0.190	-11959	0.200	—	0.231	0.200	-10481	0.191	-10607
RIT:eBBH:1740	1.00	-5.0×10^{-1}	0	26.82	0.190	-10036	0.213	—	0.226	0.213	-8540	0.201	-8677
RIT:eBBH:1899	1.00	-4.0×10^{-1}	0	28.30	0.190	-10530	0.211	—	0.222	0.211	-9033	0.203	-8837
RIT:eBBH:1514	0.20	0	0	43.30	0.190	-15722	0.201	0.217	0.223	0.201	-14227	0.194	-14024
RIT:eBBH:1353	0.80	0	0	32.46	0.190	-12005	0.199	0.216	0.220	0.199	-10524	0.190	-10652
RIT:eBBH:1422	0.50	0	0	35.11	0.190	-13016	0.201	0.218	0.220	0.201	-11534	0.193	-11335
RIT:eBBH:1537	0.17	0	0	20.90	0.190	-6209	0.195	0.207	0.192	0.196	-4795	0.193	-4953
RIT:eBBH:1701	1.00	0	7.0×10^{-1}	31.67	0.190	-11702	0.198	—	0.210	0.198	-10223	0.192	-10356
RIT:eBBH:1491	0.25	0	0	46.99	0.190	-17776	0.202	0.217	0.224	0.203	-16282	0.195	-16079
RIT:eBBH:1399	0.60	0	0	34.05	0.190	-12651	0.199	0.216	0.219	0.199	-11168	0.190	-11296
RIT:eBBH:1763	1.00	-8.0×10^{-1}	0	23.85	0.190	-8996	0.216	—	0.229	0.216	-7495	0.205	-7287
RIT:eBBH:1282	1.00	0	0	31.68	0.190	-11706	0.200	—	0.220	0.200	-10230	0.192	-10357
RIT:eBBH:1330	0.90	0	0	32.19	0.190	-11894	0.199	0.217	0.218	0.199	-10413	0.190	-10215

TABLE II. NR simulations analyzed in this paper. We refer to each run using the ID numbers reported in the SXS and RIT databases.